



Fabrication and performance analysis of A-site metal-promoted $\text{La}_{0.595}\text{V}_{0.005}\text{Sr}_{0.4}\text{CoO}_{3-\delta}$ perovskite oxides as cathodes for intermediate temperature solid oxide fuel cells

Ayşenur Eslem Kisa¹ · Oktay Demircan¹

Received: 23 November 2023 / Revised: 25 February 2024 / Accepted: 26 February 2024 / Published online: 18 March 2024
© The Author(s), under exclusive licence to Springer-Verlag GmbH Germany, part of Springer Nature 2024

Abstract

Reducing fabrication costs and increasing system performance are the primary objectives of contemporary SOFC developments and research. One of the efficient ways to address the design and durability difficulties is to lower the operating temperatures to the intermediate range (IT, 500–800 °C). $\text{La}_{0.595}\text{V}_{0.005}\text{Sr}_{0.4}\text{CoO}_{3-\delta}$ (LV05SC) perovskite cathode is investigated as a novel cathode for intermediate temperature solid oxide fuel cells (IT-SOFC). Anode-supported YSZ ($(\text{Y}_2\text{O}_3)_{0.08}(\text{ZrO}_2)_{0.92}$) and GDC ($\text{Gd}_{0.1}\text{Ce}_{0.9}\text{O}_{1.95}$) electrolytes were prepared by a multilayer tape casting and co-firing method. The green bi-layer tapes were co-fired at various temperatures with optimized electrolyte and anode slurries. X-ray Diffraction (XRD) and Scanning Electron Microscopy (SEM) were used to analyze the microstructures and the phase characterizations of the cathode material and single cell. At 1250 °C of the co-firing temperature, as-prepared anode-supported cells showed no defects and excellent microstructural properties such as no gas permeability, porosity, and sintered structure. The electrolytes with a thickness of almost 20 µm were fairly dense. The power densities were evaluated and both anode-supported electrolytes showed good electrochemical performance at intermediate temperatures. The peak power density of the cell reached 89 mW/cm², and the total resistance was only 3.05 Ω·cm² under open circuit conditions at 800 °C. The diffusion processes of oxide ions (O^{2-}) were found to be the limiting step for ORR by the EIS analysis. These findings suggest that the compound is a promising cathode material for IT-SOFCs.

Keywords Solid oxide fuel cells (SOFC) · Perovskite · Vanadium doping · Oxygen reduction reaction (ORR) · Cathode

Introduction

Low pollutant emissions and harmless byproducts improve fuel cells as one of the highly efficient and environmentally friendly energy conversion devices. Solid oxide fuel cells (SOFCs) are accepted as an electrochemical energy conversion technology that directly transforms chemical energy into electrical energy. Because of its high efficiency, adaptability to a variety of fuels, and environmental sensitivity, SOFCs have received a lot of research interest [1]. Decreasing fabrication costs and improving system stability, which are the key barriers to commercialization for fuel cells, are the primary objectives of the development of contemporary

SOFC for researchers. The materials used in both electrodes supported SOFCs, which operate in the temperature range of 800–1000 °C, should be less costly and provide fewer material compatibility issues [2]. One of the efficient ways to address the design and durability difficulties is to lower the operating temperatures to the intermediate range (IT, 600–800 °C). However, as the conventional cathode $\text{La}_{0.6}\text{Sr}_{0.4}\text{CoO}_3$ (LSC) exhibits weak catalytic activity for the oxygen reduction reaction (ORR) at low temperatures, the significant increase in cathode polarization resistance has emerged as a major problem limiting the electrochemical performance of IT-SOFCs [3]. Also, to address the design concerns, there have been many research efforts including reducing the thickness of the YSZ layer and using substitute electrolyte materials having better ionic conductivity than YSZ at low and intermediate temperatures, such as doped ceria (GDC— $\text{Gd}_{0.2}\text{Ce}_{0.8}\text{O}_{1.95}$) and doped LaGaO_3 [4–8]. Despite the reports of effective operation at low and intermediate temperatures, the best materials and methods for

✉ Oktay Demircan
oktay.demircan@boun.edu.tr

¹ Department of Chemistry, Boğaziçi University,
Bebek 34342 Istanbul, Turkey

low-cost processes producing stable and consistently high SOFC performance have not yet been fully addressed.

The ORR which is supposed to take place at triple phase boundaries (TPB), is fundamentally an electrochemical event involving charge transfer. Since Pt electrodes were the only SOFC cathode material utilized until 1965, significant studies on those electrodes have led to the realization that by increasing the size of the active zone on the electrode/electrolyte interface, it is possible to enhance the ORR kinetics at lower temperatures [9]. This inspires scientists to explore and develop the possible use of transition metal oxides, or perovskites, as SOFC cathodes [10]. Perovskites display strong ORR catalytic capabilities, chemical and thermal durability, as well as noticeable mixed electrical and ionic conductivity [11]. These perovskite materials remain also comparatively less expensive than Pt metal.

Polarization losses at the cathode caused by ORR generate the majority of the total losses in such SOFCs with thin film electrolytes. The large activation energy and slow ORR processes are responsible for the substantial cathodic polarization losses. Additionally, the migration of oxide ions inside the porous cathode is a vital factor for cell performance [3]. In practice, there are two main ways to reduce cathode polarization losses: either by selecting a cathode material composition that optimally matches the triple-phase boundary (TPB, including the ion-conducting layer, electron-conducting layer, and the gas phase) to improve oxide ion exchange and diffusion kinetics or by modifying the cathode/electrolyte interface microstructure to increase the TPB dimensions [12]. The surface and/or active area is another essential element for better performance for ORR, according to electrochemical studies on dense, porous, and porous/dense double-layered cathode materials based on LSC and LSM ($\text{La}_{1-x}\text{Sr}_x\text{CoO}_3$ and $\text{La}_{1-x}\text{Sr}_x\text{MnO}_3$, respectively) [13–20].

Mixed ionic–electronic conductors (MIECs) are designed to expand the ORR active range from the TPB to the whole air electrode surface so that the electrode reaction kinetics can be improved in order to address this problem [21]. For this purpose, perovskite cathodes, particularly based on cobalt, are the most promising preferences among MIECs because of their superior electrocatalytic activity at the IT region for the ORR [22]. By employing the incoming electrons from the anode current collector, the flowing molecular oxygen is converted to oxide ions by catalytic conversion onto the surface of the porous cathode. The location of the ORR might be close to the electrode/gas interface or on the TPB regions, depending on the characteristics of the cathode material [23]. The fuel is oxidized as a result of subsequent passage of the oxide ions to the anode (through diffusion via a dense electrolyte). By selecting the optimal composition of the constituent materials and adjusting the sintering and processing conditions to produce grains of different sizes,

modification of the cathode microstructure ultimately determines the performance of the cathode [24–26].

As a possible electrode material, perovskite oxides ABO_3 exhibit a variety of advantageous properties, such as improvement in oxygen ion mobility and higher stability of the mixed valence states of Ti, V, Nb, Mo, and other elements in the crystal structure [27–30]. By using atomic substitution/doping or non-stoichiometry on either cation or anion sub-lattices, the composition of ABO_3 may be greatly enhanced. Such modifications trigger improvements in electrical and ionic conductivities, sintering behavior, and catalytic performance. The perovskite structure offers an a priori choice of the active site crucial to catalysis when an inactive A-site ion (like La^{3+} or Sr^{3+}) is combined with an active B-site ion (like Co^{3+} , Mn^{3+} , or Ti^{3+}). Additionally, the selection of the A-cation can change the characteristics of the B-cation and its nearby oxygen ions [31]. By doping vanadium metal to the A-site, the oxide electroneutrality and charge compensation mechanism suggest that the negative charge defect caused by Sr^{2+} replacing La^{3+} at the A-site is compensated for by aliovalent V ions. V^{4+} and V^{5+} are the two key oxidation states which are proved by X-ray Photoelectron Spectroscopy (XPS) analysis [32, 33]. So, the continuous conduction of electrons through B-O-B and V-O-V saddle points is made possible by shared electron pairs of $\text{B}^{3+}/\text{B}^{4+}$ and $\text{V}^{4+}/\text{V}^{5+}$. Vanadium-doped perovskites of LSF by Zhang and co-workers have shown also that the V 2p peak in XPS was split into two peaks V^{4+} and V^{5+} , which correspond to the binding energies 515.8 eV and 516.8 eV; hence, the existence of the shared electron pair of as $\text{V}^{4+}/\text{V}^{5+}$ has enabled the continuous conduction of electrons through V-O-V [34]. Vanadium-doped perovskites of LSF by Zhang and co-workers have shown also that the existence of the shared electron pair of as $\text{V}^{4+}/\text{V}^{5+}$ has enabled the continuous conduction of electrons through V-O-V.

The attempt to lower the operating temperature from 800 to 600 °C or below is one of the primary research goals in this area. The benefits of SOFCs operating at lower temperatures include a larger selection of materials, improved long-term performance, system compactness, and perhaps lower fuel cell costs [12, 35]. To address these concerns, there have been many research efforts including reducing the thickness of the YSZ layer and using substitute electrolyte materials having better ionic conductivity than YSZ at low and intermediate temperatures, such as doped ceria (GDC— $\text{Gd}_{0.2}\text{Ce}_{0.8}\text{O}_{1.95}$) and doped LaGaO_3 [4–8]. Despite the reports of effective operation at low and intermediate temperatures, the best materials and methods for low-cost processes producing stable and consistently high SOFC performance have not yet been fully addressed.

Preceded research about LV05SC revealed that replacing vanadium with A-site metals clearly enhanced the electrical conductivity of perovskite material [28, 29]. Findings

about LV05SC with good electro-catalytic activity for ORR presented a potential cathode material for IT-SOFC applications. The effects of these enhancements in the chemical and physical properties of perovskite with vanadium-doping to A-site in this study were investigated for the first time to understand the ORR mechanism in the operation of SOFC on the intermediate temperature range. The tape casting and co-firing procedures were employed to produce the single cell with anode-supported thin electrolytes to enhance the electrical characteristics of perovskite materials. Both electrical and ionic conductivities of perovskite materials have been measured for different temperatures and operating overpotentials by employing Electrochemical Impedance Spectroscopy (EIS). As a result of these analyses, adsorption, dissociation, and diffusion processes were found to be the rate-limiting steps of ORR. These findings suggest that this V-doped perovskite structure, LV05SC, is a promising cathode material for IT-SOFCs.

Materials and methods

Material synthesis

Utilizing the sol-gel method, $\text{La}_{0.6-x}\text{V}_x\text{Sr}_{0.4}\text{CoO}_{3-\delta}$ (LV_xSC, $x=0.005$) powders were produced. Reagents included La, Sr, and Co nitrates as well as V acetate (purity > 99.9%, Aldrich Chemicals, USA). Separately, each reagent was dissolved in distilled deionized water at the proper stoichiometric ratio. To produce a homogenous solution, all of the solutions were afterward combined and agitated. As complexation and polymerization agents, ethylene glycol and citric acid, in varying amounts, were added after they had completely dissolved.

The citric acid to total metal ions ratio was maintained at approximately 1:2. The solution was allowed to evaporate on a hotplate upon prolonged heating; the gel spontaneously burned, transforming into a light and delicate ash. Following a gentle heating-induced gelation, the resulting gel was placed in a drying oven at 500 °C for 2 h to eliminate organic components. Subsequently, it was subjected to sintering at 1100 °C for 3 h to yield perovskite compounds possessing satisfactory crystalline structure, as confirmed through X-ray diffraction analysis.

Characterization of materials and electrochemical measurements

On a Rigaku D/MAX-Ultima+/PC Diffractometer, the X-ray powder diffraction data for crystal structure and phase composition of the produced powders were gathered using Cu-K α radiation ($\lambda=1.54056$ Å) as the source over the range of 20–70°. To identify the crystal structure, the

collected data was compared with reference data. For SEM-FEG, Philips XL 30 at an accelerating potential of 10 kV was used to study the surface and cross-section morphology of the sintered cells. Thermo Scientific's K α surface analysis instrument was used for the XPS analysis. The surface properties of the powdered materials were captured using an Al-K α X-ray source ($h\nu=1486.6$ eV at room temperature and a 10^{-7} -Pa vacuum) with a spot size of 400 μm , and the constant pass energy values were set at 150 eV. The charge effect was calibrated using the binding energy of C1s (284.5 eV), and the energy step size was adjusted at 0.100 eV. Performance and electrochemical impedance spectra (EIS) were measured from 500 to 800 °C utilizing a self-made test setup containing gas mass flowmeters. The sintered cells were attached to a zirconia tube with a ceramic paste. The current collectors were made of Au paste and wires connected the electrodes to the testing instrument. The current–voltage (I–V) characterization was conducted with the Gamry Ref 3000 Potentiostat (Gamry Instruments, Warminster, PA, USA) using H₂ as the fuel and oxygen as the oxidant. The AC impedance data were collected with an AC signal of 10 mV in the frequency range of 1–0.1 Hz at an open circuit. The online DRT calculator (generated by the German team at RHD Instruments, GmbH) was used to determine the distribution of relaxation times (DRT) with a regularization parameter of 10^{-3} .

Fabrication of anode-supported electrolyte via tape-casting/lamination/co-firing

A two-step ball milling procedure was used to produce the slurries for tape casting. In order to give an ideal viscosity, the required amounts of plasticizers polyethylene glycol (PEG) and benzyl-butyl-phthalate (BBP) were combined in ethanol/toluene solvent mixture, and polyvinyl butyral (PVB) was used as the binder. Secondly, anode powders mixed with electrolyte samples in 50:50 wt% were added to the slurry and ball-milled again for 24 h. There were two processes in the tape casting process as well. The de-aired electrolyte and anode slurries were initially cast at a blade height of app. 10, 20, and 200 μm , respectively. The green tapes were cut into disks with a 13 mm diameter after drying for 24 h. One sheet of YSZ and GDC electrolytes and two layers of anode green tapes were stacked in order to produce anode-supported cells. The layers were assembled in random directions for relaxation of the residual internal stress and uniaxially laminated for 5 min. The laminates were subsequently co-sintered at 1250 °C in the air for 3 h after burn-out of the organic components. Following co-sintering, the cathode paste was produced using LV05SC and GDC electrolyte powder by a weight ratio of 50:50 and was brush-coated onto the electrolyte with an active area of 0.5 cm². The cathode layer was then sintered at 1100 °C for 5 h.

Results and discussion

Crystalline structure

XRD was employed to identify the phase, purity, and crystallinity of $\text{La}_{0.595}\text{V}_{0.005}\text{Sr}_{0.4}\text{CoO}_{3-\delta}$ (LV05SC) perovskite cathode material. In Fig. 1, the XRD pattern is shown for the cathode sample synthesized by the sol-gel reaction after calcination at 1100 °C for 3 h with a comparison of LSC (JSPDS #48-0121). Phase, crystallite size, and lattice parameters are calculated and also found to match with the software crystallography open database (COD). XRD pattern reveals that synthesized cathode material has a single phase (space group R-3c:167) with lattice parameters of $a, b = 5.426 \text{ \AA}$, $c = 13.240 \text{ \AA}$ and $\alpha, \beta = 90.00^\circ$, $\gamma = 120^\circ$ and a volume of 337.53 \AA^3 . All peaks in the XRD pattern are relatively sharp, indicating good incorporation into the lattice of the metal oxides used in the powder synthesis. These XRD results are similar to literature employing LSC as a cathode material [36]. XRD pattern clearly proves that as-synthesized perovskite has formed well as $\text{ABO}_{3-\delta}$ perovskite structure without any impurity.

XPS analysis

The elemental composition of the LV05SC sample examined by XPS for all possible elements in the perovskite structure, such as La 3d, V 2p, Sr 3d, Co 2p, and O 1s, has obviously existed in the crystal which is approved by the full-scan survey spectra shown in Fig. 2a. Elemental relative percentages of LV05SC cathode sample surface have been presented in Fig. 2g as La (42.96%), V (0.48%), Sr (9.37%), Co (13.46%), O (28.88), and C (4.85%); since the sample was exposed air, elemental carbon is observed.

The XPS spectrum of La 3d is shown in Fig. 2b. It has two wide peaks with a splitting of 16.7 eV, one at a lower binding energy at 833.01 eV and another at a higher binding energy at 849.71 eV, which correspond to the La 3d_{5/2} and La 3d_{3/2} spectra, respectively. The relative intensity ratio for La 3d_{5/2} and La 3d_{3/2} is around 1.38; these values are closely related to those found in the literature [37]. The difference between the La 3d_{5/2} doublet splitting, which is about 3.6 eV, confirms the existence of lanthanum hydroxides [38, 39]. As a result, the La 3d is in +3 oxidation states, as shown by the distinct separation of these spin-orbit splitting. Also, the substitution of La ions by Sr and V ions did

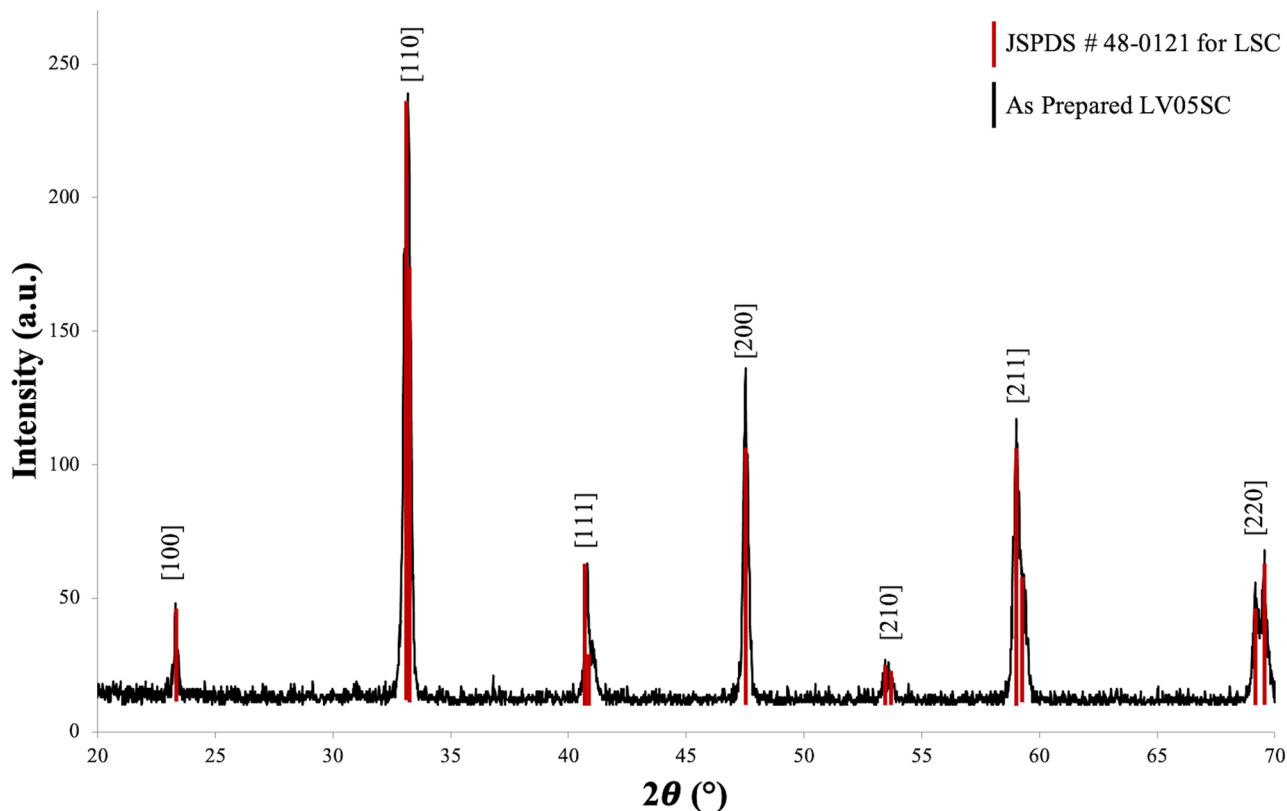


Fig. 1 XRD pattern of LV05SC cathode sample

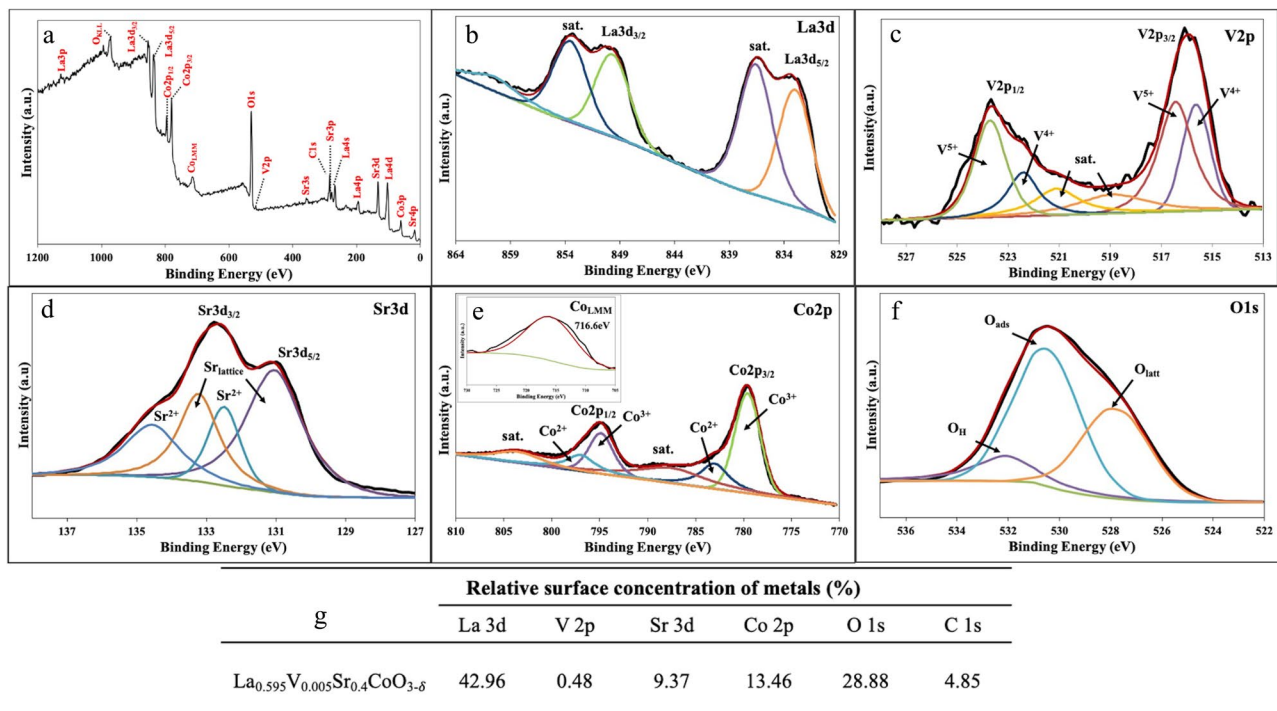


Fig. 2 XPS spectra **a** survey scan, **b** La 3d, **c** V 2p, **d** Sr 3d, **e** Co 2p, **f** O 1s, and **g** relative percentage of elements for LV05SC cathode sample

not result in any observable shift in the position of these peaks in XRD and XPS spectra.

The high-resolution XPS spectra of V 2p, which can be seen in Fig. 2c, can be deconvoluted into four peaks at 515.6, 516.4, 522.4, and 523.7 eV, which indicates the oxidation states of vanadium in this sample are +5 and +4 [40, 41]. The area ratio between the V 2p_{3/2} and V 2p_{1/2} energy levels, arising from the orbital splitting of the V 2p energy level, was set to 1.5:1, and the energy separation between the two levels was set at 7.7 eV. These results are in good agreement with the results for perovskite structure [42–44]. Additionally, the X-ray satellite of the O 1s core level is responsible for the appearance of two peaks at 518.9 and 521.1 eV [45, 46]. The three peaks at 527.8, 530.5, and 532.1 eV in the core-level O 1s spectra (Fig. 2f) can be attributed to the V-O bonding, adsorbed hydroxyl groups, and molecular water, respectively [41, 44]. According to the oxide electro-neutrality and charge compensation mechanism, the negative charge defect caused by Sr²⁺ and V⁴⁺/V⁵⁺ replacing La³⁺ at the A-site appears to be compensated for by Co³⁺. The shared electron pairs Co²⁺/Co³⁺ and V⁴⁺/V⁵⁺ allow for continuous electron transfer across Co-O-Co and V-O-V. Also, in previous research, the analysis of LV05SC with EXAFS clearly showed that V was replaced with La in the perovskite structure [32].

The Sr 3d core-level spectra were particularly helpful for determining the bulk and surface contributions in the spectra

since the Sr 3d levels had a distinct surface core-level shift [47]. The performance loss of the cathode samples in SOFC is widely known to be caused by Sr segregation, which has been confirmed by earlier studies [48, 49]. Shown in Fig. 2d, the Sr 3d spectra are well-matched using two sets of spin-orbit doublets with an energy separation of 2 eV and an area ratio of ~2. The significant peaks of the Sr 3d_{5/2} and Sr 3d_{3/2} components were seen in the spectra of the LV05SC sample at 131.0 and 133.2 eV, respectively. The contributions to the Sr 3d photoelectron spectrum were discovered to be due to perovskite lattice-bound Sr (Sr_{lattice}). The Sr atoms in Sr-OH, Sr-CO₃, Sr-Sr, and Sr-O bonds near the surface of the cathode sample (Sr_{surface}), which do not have perovskite structures, are responsible for the two additional minor peaks at 132.5 and 134.5 eV [50–54]. Since no obvious peaks assigned to carbonates could be seen in the XRD pattern in Fig. 1, the effect caused by carbonate compounds is negligible. Furthermore, the binding energies of Sr in the Sr-O structure (Sr_{surface}) and Sr in the lattice (Sr_{lattice}) are very similar, even beyond the resolution limit of this experiment configuration. The Sr_{surface} therefore most likely results from the formation of the Sr(OH)₂ phase from SrO or from the development of a Sr(OH)₂-like binding environment such as SrOH on the Sr of the perovskite lattice or on the Sr of a separated SrO phase. Even though it is clear that the Sr_{surface} associated with Sr(OH)₂ species is mostly on perovskite lattice. For the LV05SC sample, the Sr_{lattice}/Sr_{surface} ratio of 2 indicates that the Sr lattice component of the Sr 3d

occurs to a greater extent. A Sr-OH signature peak is present in the bonding environment in all three cases (Fig. 2f shows O 1s spectra that demonstrate its presence). These results are expected for a perovskite structure.

The Co 2p spectrum is divided into two distinct peaks and two weak satellites, as shown by the XPS data in Fig. 2e. Co 2p(3/2) and Co2p(1/2) might be the two spin-orbit doublets identified as cobalt oxides at 779.3 and 794.8 eV, respectively. Two peaks at 779.5 and 783.0 eV, corresponding to the Co³⁺ 2p(3/2) and Co²⁺ 2p(3/2) configurations, can be seen in the spin-orbit doublet of Co 2p(3/2). The Co 2p(1/2) spin-orbit doublet can also be divided into two different peaks that are attributed to Co³⁺ and Co²⁺ 2p(1/2), respectively, and are located at binding energies of 794.8 and 796.9 eV. The Co₃O₄ cubic phase can be identified by the Co 2p(3/2) and Co 2p(1/2) splitting energy difference of 15.5 eV. The appearance of the two satellite peaks at binding energies of 787.5 and 803.5 eV near the two spin-orbit doublets provides additional evidence for the presence of cobalt oxides. This suggests that most Cobalt ions are present as trivalent cations with a Co³⁺/Co²⁺ ratio of 2.28 [55, 56].

Since the valence of Co ions mostly forms with higher oxidation states such as Co²⁺ to Co³⁺, the oxygen vacancies are formed in the crystal structure so that the electrical neutrality of the perovskite can be maintained. A higher Co³⁺ to Co²⁺ ratio enhances the catalytic capacity of the sample surface to absorb oxygen, strengthening the Co-O bond and enhancing ORR performance. To adjust the electrocatalytic activity, Malkhandi et al. [57] carried out a comprehensive study on the perovskites. It was concluded that the catalytic activity is determined by the relative strength of the Co-O bonding. The position of the Co LMM Auger line (Fig. 2e, inset) further supports the existence of both cobalt valence states. The peak at 716.6 eV of binding energy (E_B) is equivalent to the kinetic energy of 770 eV by the equation below, and it can be used to calculate the modified Auger parameter, α :

$$\alpha = 1486.6 \text{ eV} + \text{KE}(\text{Co}_{\text{LMM}}) - \text{KE}(\text{Co}2p_{3/2}) = 1551.0 \text{ eV}$$

where KE is the kinetic energy. This value of α indicates the coexistence of Co²⁺ and Co³⁺ since it is between the given values for CoO ($\alpha = 1549.8 \text{ eV}$) and Co₃O₄ ($\alpha = 1552.9 \text{ eV}$) [58].

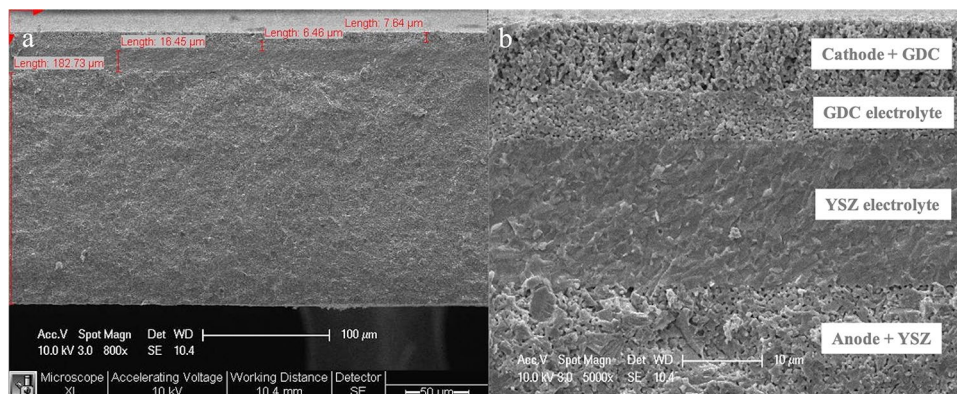
The XPS spectrum of O 1s shown in Fig. 2f exhibits two peaks, one at 530.5 eV due to adsorbed oxygen (O_{ads}) in the form of highly oxidative O⁻/O₂²⁻ species and one at 527.8 eV assigned to lattice oxygen (O_{lattice}, O²⁻) within perovskite. The extra peak at 532.1 eV, which is not always visible in O 1s spectra, is caused by the physical and chemical adsorption of molecular water or hydroxyl groups on the surface of defects [59–61].

Since lanthanum oxide has hygroscopic characteristics when exposed to air, the highest binding energy of O 1s (532.15 eV) is thought to be due to a water molecule associated with the surface lanthanum oxide. It should be noted that molecular water and surface-adsorbed oxygen in the form of hydroxyl or oxygen groups could be easily removed by heating to generate oxygen vacancies. However, removing highly oxidative oxygen species (O⁻/O₂²⁻) requires a considerably higher temperature. In most cases, the oxygen vacancies caused by the oxygen-deficient perovskite oxides can result in different oxidation states of the transition metal ions and hence increase the catalytic activity of the perovskite [62]. Also, the total amount of oxygen adsorbed in perovskite oxides corresponds to the amount of oxygen vacancies. The catalytic activity and ionic conductivity of a perovskite increases with the amount of oxygen vacancies present on its surface [63].

Surface morphology analysis of the cell

To achieve adequate energy conversion rates and provide a suitable power output, an SOFC with a thin electrolyte sheet is preferred [64]. In this study, thin YSZ and GDC electrolytes made via tape-casting were used to produce a NiO-YSZ anode-supported fuel cell. Figure 3 displays a cross-sectional SEM micrograph of an LV05SC/GDC/YSZ/NiOYSZ single

Fig. 3 SEM images of LV05SC-GDC-YSZ-NiOYSZ cell



cell. It is evident that the porous NiOYSZ anode is tightly attached to the YSZ electrolyte layer, which is quite dense and crack-free. Also, there are no cracks or delamination found between the electrolyte and the cathode layers, demonstrating a strong interfacial adhesion. The thickness of the LV05SC-GDC composite cathode can be clearly measured as 7.64 μm . The thickness of the GDC interlayer for segregation against Zr from the YSZ electrolyte is measured as 6.46 μm . Therefore, electrode polarization losses from the anode and cathode have a dominant influence on the performance of the anode-supported cell [65]. The thickness of the YSZ electrolyte layer is clearly seen as 16.45 μm with no cracks or pinholes, resulting in a low ohmic resistance [66]. The thickness of the NiO-YSZ composite anode and also physical support for the cell is around 180 μm . These thicknesses are precisely comparable with the conventional SOFC cell parameters [67–69].

Single-cell performances

The current–voltage characteristics of the SOFC with YSZ/GDC electrolytes are plotted in Fig. 4. The open circuit potential decreases from 1.1 to 0.93 V with the temperature increase from 500 to 800 $^{\circ}\text{C}$. It appeared that the electrolyte and cell seal were entirely impermeable. When compared to data from the literature, the OCV values for the GDC electrolyte thin film were the highest and the closest to the predicted values of 0.98 V found at 600 $^{\circ}\text{C}$ [70].

This demonstrated a correlation between the thick GDC electrolyte thin film and the SEM analysis. The maximum power density is 6.12, 13.27, 31.80, and 88.95 $\text{mW}\cdot\text{cm}^{-2}$ at 500, 600, 700, and 800 $^{\circ}\text{C}$, respectively. However, for a practical SOFC, the electrode resistance of the cell is too high. The pore distribution, microstructure, triple-phase boundary region, and interface between electrodes and electrolyte layers are among the factors that influence cell performance [32]. These variables control the ohmic resistance of the electrode/electrolyte interface as well as the activation and concentration resistances of the electrodes.

In the literature, the LSC-GDC composite cathode has been studied extensively. Wang and co-workers have presented that the button cell with LSC-GDC (5:5) performed well with the maximum power density value of 513 $\text{mW}\cdot\text{cm}^{-2}$ at 650 $^{\circ}\text{C}$; however, the thickness of GDC electrolyte in their cell has been less than 2 μm , and the thickness of YSZ layer has been less than 10 μm with the cathode active area of 0.5 cm^2 [71]. Another study from Solovyev and co-workers about LSC cathode has revealed that the cell with magnetron sputtered LSC-GDC composite cathode interlayer with a thickness of ~ 2 μm had the maximum power density value of 503 $\text{mW}\cdot\text{cm}^{-2}$ at 700 $^{\circ}\text{C}$ [72]. When these maximum power density values are compared to LV05SC, the thickness of the LV05SC cathode and the electrolyte layer play a crucial role in the performance due to the difficulty of oxide ion diffusion through composite cathode and electrolyte.

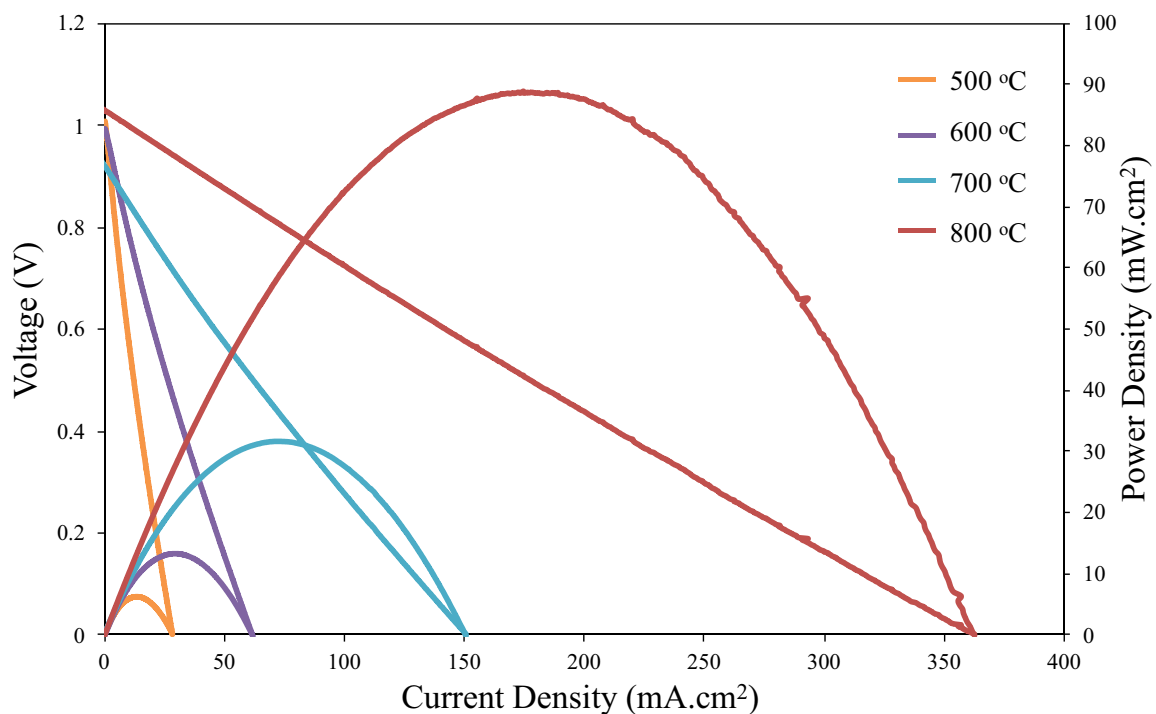


Fig. 4 I–V–P curves of the fuel cell LV05SC/GDC/YSZ/NiO-YSZ using H₂ as fuel and air as oxidant at different temperatures

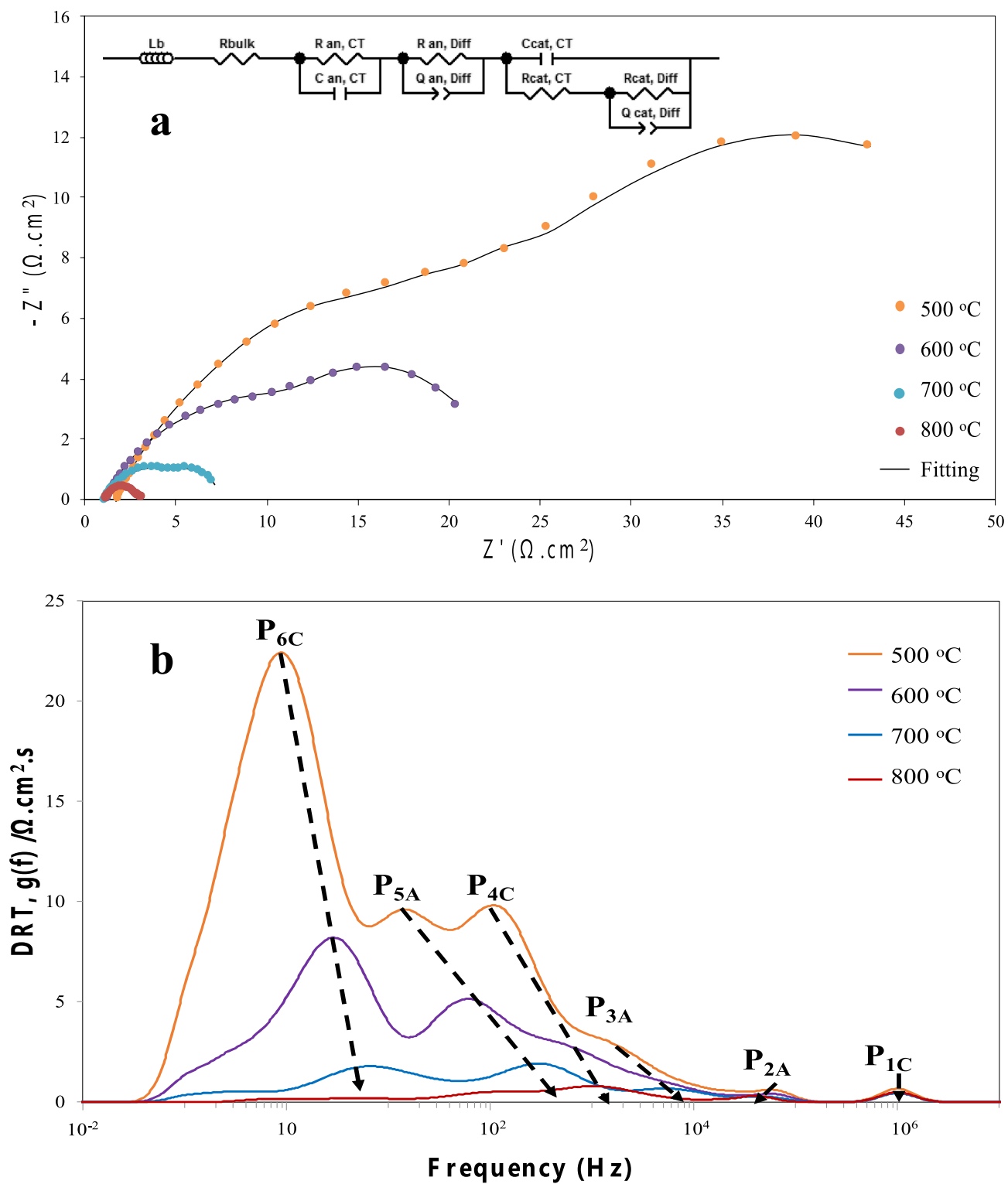


Fig. 5 Electrochemical Impedance spectroscopy (EIS) measurements single cell under open circuit conditions at different temperatures, **a** Nyquist plots (inset—equivalent circuit) and **b** DRT analysis

Electrochemical impedance spectroscopy (EIS) and distribution of relaxation time (DRT) analysis

Electrochemical impedance spectroscopy (EIS) measurements and distribution of relaxation time (DRT) analysis at the open-circuit potential for LV05SC/GDC/YSZ/NiOYSZ cell were recorded to examine the impedance and resistance dependency at the temperature range of 500–800 °C. The Nyquist plots as a function of temperature and DRT analysis of these EIS measurements are displayed in Fig. 5. The equivalent circuit used to model the experimental data is displayed in Fig. 5 inset. The values of impedance spectra on the real part of the Nyquist plot drop as the temperature increases, as expected. The asymmetrical shape of impedance plots as typical two-semicircular arcs intercepting the real axis at a frequency of ~10 kHz suggests that there are several steps taking place in this selected frequency. The entire spectra shifted toward lower values on the real and imaginary axis with an increase in operating temperature from 500 to 800 °C. This enhancement is most probable due to the improvement in the ionic conductivity and surface reactions in the fuel cell, comprising the YSZ electrolyte, GDC barrier layer, and the LV05SC-GDC electrode. Also, the observation of no performance drop during the fuel cell operation reveals good compatibility of LV05SC with the GDC electrolyte. The serial or ohmic resistance (R_{Ω}) of the cell was calculated by assessing the resistance constituent of the real part of impedance, which is the intercept at the x -axis. The ohmic resistance (R_{Ω}) of the fuel cell has a decreasing trend from 1.8 to 1.1 $\Omega\cdot\text{cm}^2$ with an increase in temperature from 500 to 800 °C. The activation barrier value of YSZ ionic conductivity is comparable when considering similar YSZ electrolyte thickness [73].

The equivalent circuit seen inset of Fig. 5a is a suitable representation for this experimental system and allows for the evaluation of EIS data. L_b , C , Q , and R in the circuit stand for inductance, capacitance, constant phase element (CPE) like pseudo capacitance, and resistance, respectively. This circuit could be explained as oxygen reduction at mixed ionic–electronic conducting cathode film essentially follows the bulk pathway, in which oxygen is first absorbed on the surface of the electrode then incorporated as oxide ion into the bulk and transported to the electrode/electrolyte phase boundary, where it eventually reaches the crystal structure of the electrolyte layer. Within the bulk pathway, the major resistive process as diffusion of oxide ion in the cathode ($R_{\text{cat, diff}}$) is the electrochemical resistance associated with oxygen exchange at the cathode surface. At low frequencies, the matching semicircle in the spectra is observed, submitting a high capacitance. This large capacitance, designated as $C_{\text{cat, diff}}$, is called chemical capacitance linked to variations in the oxygen stoichiometry in the electrode bulk. As a result, information about the oxide ion diffusion on the

surface of the cathode ($R_{\text{cat, diff}}$) and the diffusion in the bulk ($C_{\text{cat, diff}}$) are assigned to the dominant low-frequency arc. The transfer of electrons to the oxide ions across the electrode/electrolyte interface corresponds to the resistive component of medium frequency as charge transfer resistance ($R_{\text{cat, CT}}$). An interfacial capacitance connected to the same boundary is the mid-frequency capacitance as double-layer cathodic capacitance ($C_{\text{cat, DL}}$). The ohmic resistance (R_{Ω}) of the electrolyte and non-zero electrical contact resistance of gold wires are responsible for the high-frequency intercept of the impedance spectra.

Table 1 displays the variations of resistances derived from the fitted impedance data as a function of temperature. The total resistance is the sum of the ohmic resistance, the charge transfer process that occurs at the electrode/electrolyte interface, and the resistance from adsorption, dissociation, and diffusion steps of the oxygen ion on the cathode material [74]. Except for the charge transfer process in cathode, $R_{\text{cat, CT}}$, there is an obvious and known trend in resistance values as decreasing by increasing temperature. The reason for this declining tendency can be attributed to the temperature effect on processes (adsorption, dissociation, diffusion, and charge transfer) by adding kinetic energy to the reactants [75]. The increased electrochemical activity can be attributed to the increasing electrical conductivity and vacancy concentration with temperature, which improves the charge transfer and oxygen surface exchange in the cathode sample and thus improves the ORR that occurs at the cathode/electrolyte interface. However, the temperature independence of $R_{\text{cat, CT}}$ can be elucidated that the vanadium-doped cathode material LV05SC operates at all temperatures.

The activation energy (E_a) based on total resistance is equal to 1.17 eV calculated from Arrhenius equation by using EIS data shown in Fig. 5. This value is lower than that which has been reported for the single perovskite cathode materials such as $\text{La}_{0.6}\text{Sr}_{0.4}\text{FeO}_{3-\delta}$ (1.8 eV) and $\text{Ba}_{0.5}\text{Sr}_{0.5}\text{FeO}_{3-\delta}$ (1.8 eV) [76, 77]. The vanadium doping to the conventional cathode material causes this decrease in E_a since the multivalency of vanadium plays an important role in oxygen reduction reaction (ORR) [78]. Furthermore, the low-frequency resistance in total resistance exhibits greater

Table 1 Resistance values obtained from the EIS data fitted to the equivalent circuit at various temperatures (500–800 °C)

Resistances ($\Omega\cdot\text{cm}^2$)	500 °C	600 °C	700 °C	800 °C
R_{bulk}	1.06 ± 0.05	0.52 ± 0.02	0.41 ± 0.02	0.32 ± 0.02
$R_{\text{anode, CT}}$	5.36 ± 0.2	1.15 ± 0.08	0.62 ± 0.03	0.13 ± 0.01
$R_{\text{anode, diff}}$	31.29 ± 0.6	10.61 ± 0.5	2.21 ± 0.09	0.81 ± 0.03
$R_{\text{cat, CT}}$	0.57 ± 0.01	0.57 ± 0.03	0.56 ± 0.03	0.57 ± 0.02
$R_{\text{cat, diff}}$	25.26 ± 0.7	10.82 ± 0.5	4.01 ± 0.2	1.22 ± 0.06
R_T	63,54 ± 0.8	23,67 ± 0.6	7.81 ± 0.2	3,05 ± 0.2

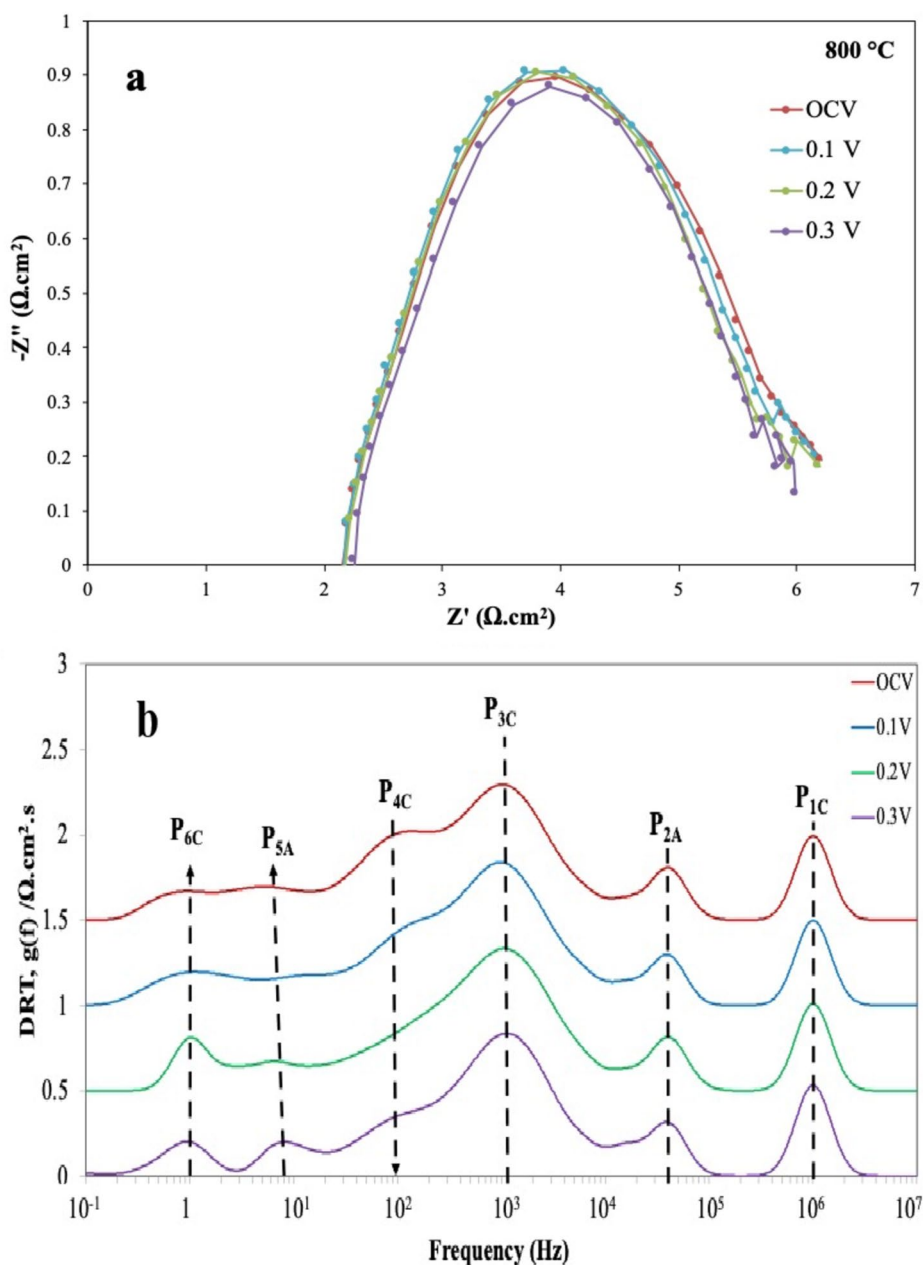
Total resistances, R_T , are given in bold. These are as important as the others, so no necessity for the "bold"

values than the high-frequency resistance in all temperature ranges. The highest contribution in total resistance at all temperatures is the diffusion of oxide ion (O^{2-}) in the cathode, $R_{cat, diff}$. This may be explained by the known striving of O^{2-} diffusion in the perovskite surface and bulk [79]. Due to these struggles, the diffusion of O^{2-} can be specified as the rate-limiting in the cathode to reduce oxygen [18, 80].

The DRT analysis of the EIS as an evaluation of operating temperature is displayed in Fig. 5b. Six polarization peaks in the frequency range of 100 kHz to 0.1 Hz were perceived, in which five peaks were discovered to be dependent upon the operating temperature of the cell, and one peak is mostly independent upon the operating temperature. These peaks displayed a drastic decrease in the polarization resistance

with a rise of the temperature from 500 to 800 °C, signifying whichever relaxation processes related to these peaks were improved while increasing temperature. Correspondingly, the peak at highest frequency with no change in frequency is related to charge transfer in cathode (P_{1C}), the peak at second highest frequency with a slight shift to the lower frequency with an increase in temperature is related to charge transfer in the anode (P_{2A}), and the four other peaks (P_{3A} , P_{4C} , P_{5A} , and P_{6C}) illustrate a common shift from the low frequency to the high frequency with a rise in temperature because of a decrease in resistance. The peak labeled as P_{3A} is related to the diffusion of H^+ ions in the anode. Another peak labeled as P_{4C} is related to the diffusion of O^{2-} ion since it is drastically diminished by an increase in temperature. The peaks at

Fig. 6 Electrochemical impedance spectroscopy (EIS) measurements of a single cell under OCV and different operating overpotentials with respect to OCV at 800 °C; **a** Nyquist plots, and **b** DRT analysis



lower frequencies are assigned to P_{5A} , and P_{6C} by a distinct thermal activation reaction of hydrogen (P_{5A}) and oxygen (P_{6C}) [79, 81, 82].

The P_{1C} peak with no change in frequency and intensity by increasing operating temperature infers that the charge transfer resistance in the cathode is independent of operating temperature. Also, the charge transfer resistance in the anode as the P_{2A} peak is slightly decreased and shifted to the lower frequency, which can be concluded that the temperature-dependent balance between Ni and NiO in the anode has a positive effect on the charge transfer process. The reduction of diffusion resistances of H^+ (P_{3A}) and O^{2-} (P_{4C}) ions is well-known due to the increase in kinetic energy of these ions with a rise in temperature. The thermal activation resistances of hydrogen (P_{5A}) and oxygen (P_{6C}) are diminished by increasing operating temperature due to the positive effect of temperature in lowering the activation energy of hydrogen (P_{5A}) and oxygen (P_{6C}) bonds.

EIS measurements and DRT analysis of a single cell under OCV and different operating overpotentials at 800 °C are displayed in Fig. 6. Although no significant change can be perceived in EIS measurements, DRT analysis in Fig. 6b reveals the dependencies of the resistive processes in the cell. There are six distinctive peaks seen in DRT analysis. The P_{1C} , P_{2A} , and P_{3A} peaks are independent of the increase in operating overpotential due to the nature of these processes attributed, since the charge transfer resistances and diffusion of H^+ ion are independent in this working potential range. However, the slight decrease in the P_{4C} peak with a rise in overpotential is observed due to the benefit of higher current in the diffusion of O^{2-} ion while increasing working overpotential. On the other hand, the increase in activation resistances of hydrogen (P_{5A}) and oxygen (P_{6C}), respectively, is related to complications and mildness of breaking hydrogen and oxygen bonds with higher current while increasing working overpotential. According to the analysis of these EIS data with variations in operating temperature and overpotential, the diffusion of oxide ion (O^{2-}) in the cathode is the reason for the limited performance of the fuel cell. The optimization of the cathode can be achieved by enhancing the diffusion of ions in the fuel cell.

Conclusions

$La_{0.595}V_{0.005}Sr_{0.4}CoO_{3-\delta}$ (LV05SC) perovskite was synthesized by the sol–gel method and evaluated as a cathode material for IT-SOFC in this study. The synthesized powder exhibits a perovskite structure as the single-phase perovskite crystal with a rhombohedral lattice structure and space group of R-3cH. Since there is no performance drop during the fuel cell operation, it is determined that LV05SC shows good compatibility with the GDC electrolyte sample. The XPS analysis shows the presence of V^{4+}/V^{5+} , and the partial

substitution of vanadium into the A-site seems to be compensated by Co^{2+}/Co^{3+} . The shared electron pairs Co^{2+}/Co^{3+} and V^{4+}/V^{5+} enable continuous electron flow between Co-O-Co and V-O-V and better performance of the cathode. According to the analysis of EIS data with variations in operating temperature and overpotential, the diffusion of oxide ion (O^{2-}) in the cathode is the limiting step for ORR. These findings suggest that $La_{0.595}V_{0.005}Sr_{0.4}CoO_{3-\delta}$ (LV05SC) perovskite is a promising cathode material for IT-SOFCs. Advances in the diffusion processes of ions in the materials would promote the performance and optimization of fuel cells.

Author contribution Ayşenur Eslem Kısa: Conceptualization, validation, investigation, formal analysis, writing—original draft, visualization, and writing—review and editing. Oktay Demircan: Conceptualization, writing—review and editing, and supervision.

Funding This research received funding from Boğaziçi University Research Funds (grant numbers: 19B05D5 and 22B05D5).

Data availability The authors do not have permission to share data.

Declarations

Competing interests The authors declare no competing interests.

References

1. Singhal S, Kendall K (2003) High temperature solid oxide fuel cells: fundamentals, design and applications. Elsevier, Oxford
2. Ormerod RM (2003) Solid oxide fuel cells. Chem Soc Rev 32:17–28. <https://doi.org/10.1039/b105764m>
3. Adler SB (2004) Factors governing oxygen reduction in solid oxide fuel cell cathodes. Chem Rev 104:4791–4844. <https://doi.org/10.1021/cr020724o>
4. Kim C, Kim J, Shin J, Kim G (2014) Effects of composite cathode on electrochemical and redox properties for intermediate-temperature solid oxide fuel cells. Int J Hydrogen Energy 39:20812–20818. <https://doi.org/10.1016/j.ijhydene.2014.07.007>
5. Choi S, Yoo S, Kim J, Park S, Jun A, Sengodan S, Kim J, Shin J, Jeong HY, Choi Y, Kim G, Liu M (2013) Highly efficient and robust cathode materials for low-temperature solid oxide fuel cells: $PrBa_{0.5}Sr_{0.5}Co_{2-x}Fe_{xO_{5+\delta}}$. Sci Rep 3:2426. <https://doi.org/10.1038/srep02426>
6. Ralph JM, Schoeler AC, Krumpelt M (2001) Materials for lower temperature solid oxide fuel cells. J Mater Sci 36:1161–1172. <https://doi.org/10.1023/A:1004881825710>
7. Choi S, Shin J, Ok KM, Kim G (2012) Chemical compatibility, redox behavior, and electrochemical performance of Nd1–Sr CoO3– cathodes based on Ce1.9Gd0.1O1.95 for intermediate-temperature solid oxide fuel cells. Electrochim Acta 81:217–223. <https://doi.org/10.1016/j.electacta.2012.07.090>
8. Park S, Choi S, Kim J, Shin J, Kim G (2012) Strontium doping effect on high-performance $PrBa_{1-x}Sr_xCo_2O_{5+}$ as a cathode material for IT-SOFCs. ECS Electrochem Lett 1:F29–F32. <https://doi.org/10.1149/2.007205eel>
9. La O' GJ, Yildiz B, McEuen S, Shao-Horn Y (2007) Probing oxygen reduction reaction kinetics of Sr-Doped $LaMnO_3$ supported on Y_2O_3 -stabilized ZrO_2 : EIS of Dense, Thin-Film Microelectrodes. J Electrochem Soc 154:B427. <https://doi.org/10.1149/1.2508887>

10. Zhi M, Mariani N, Gemmen R, Gerdes K, Wu N (2011) Nanofiber scaffold for cathode of solid oxide fuel cell. *Energy Environ Sci* 4:417–420. <https://doi.org/10.1039/C0EE00358A>
11. Jun A, Kim J, Shin J, Kim G (2016) Perovskite as a cathode material: a review of its role in solid-oxide fuel cell technology. *ChemElectroChem* 3:511–530. <https://doi.org/10.1002/celec.201500382>
12. Steele BCH, Heinzel A (2001) Materials for fuel-cell technologies. *Nature* 414:345–352. <https://doi.org/10.1038/35104620>
13. Tietz F, Arulraj I, Zahid M, Stover D (2006) Electrical conductivity and thermal expansion of $\text{La}_{0.8}\text{Sr}_{0.2}(\text{Mn}, \text{Fe}, \text{Co})\text{O}_{3-\delta}$ perovskites. *Solid State Ion* 177:1753–1756. <https://doi.org/10.1016/j.ssi.2005.12.017>
14. Tai LW (1995) Structure and electrical properties of $\text{La}_{1-x}\text{Sr}_x\text{Co}_{1-y}\text{Fe}_y\text{O}_3$. Part 1. The system $\text{La}_{0.8}\text{Sr}_{0.2}\text{Co}_{1-y}\text{Fe}_y\text{O}_3$. *Solid State Ion* 76:259–271. [https://doi.org/10.1016/0167-2738\(94\)00244-M](https://doi.org/10.1016/0167-2738(94)00244-M)
15. Yamamoto O (1987) Perovskite-type oxides as oxygen electrodes for high temperature oxide fuel cells. *Solid state ion* 22:241–246. [https://doi.org/10.1016/0167-2738\(87\)90039-7](https://doi.org/10.1016/0167-2738(87)90039-7)
16. Petrov A (1995) Crystal structure, electrical and magnetic properties of $\text{La}_{1-x}\text{Sr}_x\text{CoO}_3 - y$. *Solid State Ion* 80:189–199. [https://doi.org/10.1016/0167-2738\(95\)00114-L](https://doi.org/10.1016/0167-2738(95)00114-L)
17. Kawada T, Suzuki J, Sase M, Kaimai A, Yashiro K, Nigara Y, Mizusaki J, Kawamura K, Yugami H (2002) Determination of oxygen vacancy concentration in a thin film of $\text{La}_{[0.6]}\text{Sr}_{[0.4]}\text{CoO}_{[3-\delta]}$ by an electrochemical method. *J Electrochem Soc* 149:E252. <https://doi.org/10.1149/1.1479728>
18. Jiang S (2002) A comparison of O₂ reduction reactions on porous (La, Sr)MnO₃ and (La, Sr)(Co, Fe)O₃ electrodes. *Solid state ion* 146:1–22. [https://doi.org/10.1016/S0167-2738\(01\)00997-3](https://doi.org/10.1016/S0167-2738(01)00997-3)
19. Jiang SP, Wang W (2005) Fabrication and performance of GDC-impregnated (La, Sr)MnO₃ cathodes for intermediate temperature solid oxide fuel cells. *J Electrochem Soc* 152:A1398. <https://doi.org/10.1149/1.1928167>
20. Perry Murray E (2001) (La, Sr)MnO₃–(Ce, Gd)O₂–x composite cathodes for solid oxide fuel cells. *Solid state ion* 143:265–273. [https://doi.org/10.1016/S0167-2738\(01\)00871-2](https://doi.org/10.1016/S0167-2738(01)00871-2)
21. Taskin AA, Lavrov AN, Ando Y (2005) Achieving fast oxygen diffusion in perovskites by cation ordering. *Appl Phys Lett* 86:091910. <https://doi.org/10.1063/1.1864244>
22. Sansom JEH, Kendrick E, Rudge-Pickard HA, Islam MS, Wright AJ, Slater PR (2005) Synthesis and characterisation of the perovskite-related cuprate phases $\text{YSr}_2\text{Cu}_2\text{MO}_7+y$ (M = Co, Fe) for potential use as solid oxide fuel cell cathode materials. *J Mater Chem* 15:2321. <https://doi.org/10.1039/b502641e>
23. Wan J, Goodenough J, Zhu J (2007) $\text{Nd}_{2-x}\text{La}_x\text{NiO}_{4+\delta}$, a mixed ionic/electronic conductor with interstitial oxygen, as a cathode material. *Solid state ion* 178:281–286. <https://doi.org/10.1016/j.ssi.2007.01.013>
24. Xia C (2002) $\text{Sm}_{0.5}\text{Sr}_{0.5}\text{CoO}_3$ cathodes for low-temperature SOFCs. *Solid State Ion* 149:11–19. [https://doi.org/10.1016/S0167-2738\(02\)00131-5](https://doi.org/10.1016/S0167-2738(02)00131-5)
25. Shao Z, Haile SM (2004) A high-performance cathode for the next generation of solid-oxide fuel cells. *Nature* 431:170–173. <https://doi.org/10.1038/nature02863>
26. Peña-Martínez J, Marrero-López D, Pérez-Coll D, Ruiz-Morales JC, Núñez P (2007) Performance of XSCoF (X=Ba, La and Sm) and LSCrX (X=Mn, Fe and Al) perovskite-structure materials on LSGM electrolyte for IT-SOFC. *Electrochim Acta* 52:2950–2958. <https://doi.org/10.1016/j.electacta.2006.09.004>
27. Hansen K, Hansen K (2007) A-site deficient $(\text{La}_{0.6}\text{Sr}_{0.4})_{1-s}\text{Fe}_{0.8}\text{Co}_{0.2}\text{O}_{3-\delta}$ perovskites as SOFC cathodes. *Solid State Ion* 178:1379–1384. <https://doi.org/10.1016/j.ssi.2007.07.012>
28. Hansen KK, Søjgaard M, Mogensen M (2007) $\text{Gd}_{0.6}\text{Sr}_{0.4}\text{Fe}_{0.8}\text{Co}_{0.2}\text{O}_{3-\delta}$: a novel type of SOFC cathode. *Electrochem Solid-State Lett* 10:B119. <https://doi.org/10.1149/1.2743140>
29. Bebelis S, Kotsionopoulos N, Mai A, Tietz F (2006) Electrochemical characterization of perovskite-based SOFC cathodes. *J Appl Electrochem* 37:15–20. <https://doi.org/10.1007/s10800-006-9215-y>
30. Lee KT, Manthiram A (2006) Comparison of $\text{Ln}_{0.6}\text{Sr}_{0.4}\text{CoO}_{3-\delta}$ (Ln=La, Pr, Nd, Sm, and Gd) as cathode materials for intermediate temperature solid oxide fuel cells. *J Electrochem Soc* 153:A794. <https://doi.org/10.1149/1.2172572>
31. Taskin AA, Lavrov AN, Ando Y (2007) Fast oxygen diffusion in A-site ordered perovskites. *Prog Solid State Chem* 35:481–490. <https://doi.org/10.1016/j.progsolidstchem.2007.01.014>
32. Eslem Kisa A, Demircan O (2017) Synthesis and characterization of $\text{La}_{0.595}\text{V}_{0.005}\text{Sr}_{0.4}\text{CoO}_{3-\delta}$ as a novel cathode material for solid oxide fuel cells (SOFC). *J Solgel Sci Technol* 82:352–362. <https://doi.org/10.1007/s10971-017-4334-y>
33. Kisa AE, Demircan O (2017) Erratum to: synthesis and characterization of $\text{La}_{0.595}\text{V}_{0.005}\text{Sr}_{0.4}\text{CoO}_{3-\delta}$ as a novel cathode material for solid oxide fuel cells (SOFC). *J Solgel Sci Technol* 82:352–362. <https://doi.org/10.1007/s10971-017-4393-0>
34. Chen X, Hao S, Lu T, Li M, Han L, Dong P, Xiao J, Zeng X, Zhang Y (2022) A vanadium-doped $\text{La}_{0.5}\text{Sr}_{0.5}\text{FeO}_{3-\delta}$ perovskite as a promising anode of direct carbon solid oxide fuel cells for brown coal utilization. *J Alloys Compd* 928:167212. <https://doi.org/10.1016/j.jallcom.2022.167212>
35. Brandon NP, Skinner S, Steele BCH (2003) Recent advances in materials for fuel cells. *Annu Rev Mater Res* 33:183–213. <https://doi.org/10.1146/annurev.matsci.33.022802.094122>
36. Samat AA, Jais AA, Somalu MR, Osman N, Muchtar A, Lim KL (2018) Electrical and electrochemical characteristics of $\text{La}_{0.6}\text{Sr}_{0.4}\text{CoO}_{3-\delta}$ cathode materials synthesized by a modified citrate-EDTA sol-gel method assisted with activated carbon for proton-conducting solid oxide fuel cell application. *J Solgel Sci Technol* 86:617–630. <https://doi.org/10.1007/s10971-018-4675-1>
37. Mickevičius S, Grebinskij S, Bondarenka V, Vengalis B, Šliuzienė K, Orłowski BA, Osinniy V, Drube W (2006) Investigation of epitaxial LaNiO_{3-x} thin films by high-energy XPS. *J Alloys Compd* 423:107–111. <https://doi.org/10.1016/j.jallcom.2005.12.038>
38. Li JPH, Zhou X, Pang Y, Zhu L, Vovk EI, Cong L, van Bavel AP, Li S, Yang Y (2019) Understanding of binding energy calibration in XPS of lanthanum oxide by *in situ* treatment. *Phys Chem Chem Phys* 21:22351–22358. <https://doi.org/10.1039/C9CP04187G>
39. Bin Yousaf A, Imran M, Farooq M, Kasak P (2018) Interfacial Phenomenon and nanostructural enhancements in palladium loaded lanthanum hydroxide nanorods for heterogeneous catalytic applications. *Sci Rep* 8:4354. <https://doi.org/10.1038/s41598-018-22800-0>
40. Iwanaga S, Marciniak M, Darling RB, Ohuchi FS (2007) Thermopower and electrical conductivity of sodium-doped V_2O_5 thin films. *J Appl Phys* 101:123709. <https://doi.org/10.1149/1.2266160>
41. Bondarenka V, Martunas Z, Kaciulis S, Pandolfi L (2003) Sol-gel synthesis and XPS characterization of sodium–vanadium oxide bronze thin films. *J Electron Spectrosc Relat Phenomena* 131–132:99–103. [https://doi.org/10.1016/S0368-2048\(03\)00110-5](https://doi.org/10.1016/S0368-2048(03)00110-5)
42. Biesinger MC, Lau LWM, Gerson AR, Smart RStC (2010) Resolving surface chemical states in XPS analysis of first row transition metals, oxides and hydroxides: Sc, Ti, V, Cu and Zn. *Appl Surf Sci* 257:887–898. <https://doi.org/10.1016/j.apsusc.2010.07.086>
43. Silversmit G, Depla D, Poelman H, Marin GB, De Gryse R (2004) Determination of the V2p XPS binding energies for different vanadium oxidation states (V⁵⁺ to V⁰⁺). *J Electron Spectrosc Relat Phenomena* 135:167–175. <https://doi.org/10.1016/j.elspec.2004.03.004>

44. Silversmit G, Depla D, Poelman H, Marin GB, De Gryse R (2006) An XPS study on the surface reduction of V₂O₅(001) induced by Ar⁺ ion bombardment. *Surf Sci* 600:3512–3517. <https://doi.org/10.1016/j.susc.2006.07.006>
45. Yamada H, Ueda Y (1999) Magnetic, electric and structural properties of β -A_xV₂O₅ (A = Na, Ag). *J Physical Soc Japan* 68:2735–2740. <https://doi.org/10.1143/JPSJ.68.2735>
46. Shahid M, Liu J, Ali Z, Shakir I, Warsi MF (2013) Structural and electrochemical properties of single crystalline MoV₂O₈ nanowires for energy storage devices. *J Power Sources* 230:277–281. <https://doi.org/10.1016/j.jpowsour.2012.12.033>
47. Sekiyama A, Kasai S, Tsunekawa M, Ishida Y, Sing M, Irizawa A, Yamasaki A, Imada S, Muro T, Saitoh Y, Ōnuki Y, Kimura T, Tokura Y, Suga S (2004) Technique for bulk ferromiology by photoemission applied to layered ruthenates. *Phys Rev B* 70:060506. <https://doi.org/10.1103/PhysRevB.70.060506>
48. Yokokawa H, Tu H, Iwanschitz B, Mai A (2008) Fundamental mechanisms limiting solid oxide fuel cell durability. *J Power Sources* 182:400–412. <https://doi.org/10.1016/j.jpowsour.2008.02.016>
49. Simner SP, Anderson MD, Engelhard MH, Stevenson JW (2006) Degradation mechanisms of La–Sr–Co–Fe–O₃ SOFC cathodes. *Electrochem Solid-State Lett* 9:A478. <https://doi.org/10.1149/1.2266160>
50. Kim YS, Yun DJ, Kim SH, Kyoung YK, Heo S (2016) Damage-free and atomically precise surface preparation of SrTiO₃. *Curr Appl Phys* 16:1464–1467. <https://doi.org/10.1016/j.cap.2016.08.015>
51. Chen Y, Jung W, Cai Z, Kim JJ, Tuller HL, Yildiz B (2012) Impact of Sr segregation on the electronic structure and oxygen reduction activity of SrTi_{1-x}Fe_xO₃ surfaces. *Energy Environ Sci* 5:7979. <https://doi.org/10.1039/c2ee21463f>
52. Pitale SS, Nagpure IM, Kumar V, Ntwaeaborwa OM, Terblans JJ, Swart HC (2011) Investigations on the low voltage cathodoluminescence stability and surface chemical behaviour using Auger and X-ray photoelectron spectroscopy on LiSrBO₃:Sm³⁺ phosphor. *Mater Res Bull* 46:987–994. <https://doi.org/10.1016/j.materresbull.2011.03.022>
53. Bertacco R, Contour JP, Barthélemy A, Olivier J (2002) Evidence for strontium segregation in La_{0.7}Sr_{0.3}MnO₃ thin films grown by pulsed laser deposition: consequences for tunnelling junctions. *Surf Sci* 511:366–372. [https://doi.org/10.1016/S0039-6028\(02\)01546-7](https://doi.org/10.1016/S0039-6028(02)01546-7)
54. Cai Z, Kubicek M, Fleig J, Yildiz B (2012) Chemical heterogeneities on La_{0.6}Sr_{0.4}CoO_{3-δ} thin films—correlations to cathode surface activity and stability. *Chem Mater* 24:1116–1127. <https://doi.org/10.1021/cm203501u>
55. Wang C, Zhang C, Hua W, Guo Y, Lu G, Gil S, Giroir-Fendler A (2017) Catalytic oxidation of vinyl chloride emissions over Co–Ce composite oxide catalysts. *Chem Eng J* 315:392–402. <https://doi.org/10.1016/j.cej.2017.01.007>
56. Huang Q, Zhang J, He Z, Shi P, Qin X, Yao W (2017) Direct fabrication of lamellar self-supporting Co₃O₄/N/C peroxy-monosulfate activation catalysts for effective aniline degradation. *Chem Eng J* 313:1088–1098. <https://doi.org/10.1016/j.cej.2016.11.002>
57. Malkhandi S, Trinh P, Manohar AK, Manivannan A, Balasubramanian M, Prakash GKS, Narayanan SR (2015) Design insights for tuning the electrocatalytic activity of perovskite oxides for the oxygen evolution reaction. *The Journal of Physical Chemistry C* 119:8004–8013. <https://doi.org/10.1021/jp512722x>
58. Moreno-Tost R, Santamaría-González J, Maireles-Torres P, Rodríguez-Castellón E, Jiménez-López A (2002) Cobalt supported on zirconium doped mesoporous silica: a selective catalyst for reduction of NO with ammonia at low temperatures. *Appl Catal B* 38:51–60. [https://doi.org/10.1016/S0926-3373\(02\)00026-7](https://doi.org/10.1016/S0926-3373(02)00026-7)
59. Miao J, Sunarso J, Su C, Zhou W, Wang S, Shao Z (2017) SrCo_{1-x}Ti_xO_{3-δ} perovskites as excellent catalysts for fast degradation of water contaminants in neutral and alkaline solutions. *Sci Rep* 7:44215. <https://doi.org/10.1038/srep44215>
60. Yao C, Meng J, Liu X, Zhang X, Meng F, Wu X, Meng J (2017) Effects of Bi doping on the microstructure, electrical and electrochemical properties of La_{2-x}Bi_xCu_{0.5}Mn_{1.5}O₆ (x = 0, 0.1 and 0.2) perovskites as novel cathodes for solid oxide fuel cells. *Electrochim Acta* 229:429–437. <https://doi.org/10.1016/j.electacta.2017.01.153>
61. Cheng G, Kou T, Zhang J, Si C, Gao H, Zhang Z (2017) O₂-functionalized oxygen-deficient Co₃O₄ nanorods as high performance supercapacitor electrodes and electrocatalysts towards water splitting. *Nano Energy* 38:155–166. <https://doi.org/10.1016/j.nanoen.2017.05.043>
62. Maluf SS, Nascente PAP, Afonso CRM, Assaf EM (2012) Study of La_{2-x}CaxCuO₄ perovskites for the low temperature water gas shift reaction. *Appl Catal A Gen* 413–414:85–93. <https://doi.org/10.1016/j.apcata.2011.10.047>
63. Tang X, Gao F, Xiang Y, Yi H, Zhao S, Liu X, Li Y (2015) Effect of potassium-precursor promoters on catalytic oxidation activity of Mn–CoO_x catalysts for NO removal. *Ind Eng Chem Res* 54:9116–9123. <https://doi.org/10.1021/acs.iecr.5b02062>
64. Beckel D, Bieberle-Hütter A, Harvey A, Infortuna A, Muecke UP, Prestat M, Rupp JLM, Gauckler LJ (2007) Thin films for micro solid oxide fuel cells. *J Power Sources* 173:325–345. <https://doi.org/10.1016/J.JPOWSOUR.2007.04.070>
65. Jiang SP (2006) A review of wet impregnation—an alternative method for the fabrication of high performance and nanostructured electrodes of solid oxide fuel cells. *Mater Sci Eng A* 418:199–210. <https://doi.org/10.1016/j.msea.2005.11.052>
66. de Souza S, Visco SJ, De Jonghe LC (1997) Reduced-temperature solid oxide fuel cell based on YSZ thin-film electrolyte. *J Electrochem Soc* 144:L35–L37. <https://doi.org/10.1149/1.1837484>
67. Moon H, Kim S, Hyun S, Kim H (2008) Development of IT-SOFC unit cells with anode-supported thin electrolytes via tape casting and co-firing. *Int J Hydrogen Energy* 33:1758–1768. <https://doi.org/10.1016/j.ijhydene.2007.12.062>
68. Jacques-Bédard X, Napporn TW, Roberge R, Meunier M (2006) Performance and ageing of an anode-supported SOFC operated in single-chamber conditions. *J Power Sources* 153:108–113. <https://doi.org/10.1016/j.jpowsour.2005.03.138>
69. Petrovsky V, Suzuki T, Jasinski P, Anderson HU (2005) Low-temperature processed anode for solid oxide fuel cells. *Electrochem Solid-State Lett* 8:A341. <https://doi.org/10.1149/1.1928237>
70. Matsui T, Kosaka T, Inaba M, Mineshige A, Ogumi Z (2005) Effects of mixed conduction on the open-circuit voltage of intermediate-temperature SOFCs based on Sm-doped ceria electrolytes. *Solid state ion* 176:663–668. <https://doi.org/10.1016/j.ssi.2004.10.010>
71. Fan H, Liu Z, Wu Y, Wang Q, Yang J, Guan W, Han L, Wang J (2024) Electrochemical performance of La_{0.6}Sr_{0.4}CoO_{3-δ}-Ce_{0.9}Gd_{0.1}O_{1.95} composite cathode for IT-SOFCs. *Int J Appl Ceram Technol* 21:289–298. <https://doi.org/10.1111/ijac.14490>
72. Solovyev AA, Shipilova AV, Rabotkin SV, Smolyanskiy EA, Shmakov AN (2022) Magnetron sputtered LSC-GDC composite cathode interlayer for intermediate-temperature solid oxide fuel cells. *Int J Hydrogen Energy* 47:37967–37977. <https://doi.org/10.1016/j.ijhydene.2022.08.281>
73. Joong Yoon K, Biswas M, Kim H-J, Park M, Hong J, Kim H, Son J-W, Lee J-H, Kim B-K, Lee H-W (2017) Nano-tailoring of infiltrated catalysts for high-temperature solid oxide regenerative fuel cells. *Nano Energy* 36:9–20. <https://doi.org/10.1016/j.nanoen.2017.04.024>
74. Wang WB, Cao XB, Gao WJ, Zhang F, Wang HT, Ma GL (2010) Ammonia synthesis at atmospheric pressure using a reactor with thin solid electrolyte BaCe_{0.85}Y_{0.15}O_{3-α} membrane. *J Memb Sci* 360:397–403. <https://doi.org/10.1016/j.memsci.2010.05.038>

75. Huang Q-A, Hui R, Wang B, Zhang J (2007) A review of AC impedance modeling and validation in SOFC diagnosis. *Electrochim Acta* 52:8144–8164. <https://doi.org/10.1016/j.electacta.2007.05.071>
76. Baral AK, Tsur Y, Thangadurai V (2019) Electrochemical studies of Ruddlesden-Popper layered perovskite-type $\text{La}_{0.6}\text{Sr}_{1.4}\text{Co}_{0.2}\text{Fe}_{0.8}\text{O}_{4+\delta}$ cathode for solid oxide fuel cells and associated electrical loss phenomena. *Ceram Int* 45:1641–1650. <https://doi.org/10.1016/j.ceramint.2018.10.041>
77. Perry Murray E (2002) Electrochemical performance of (La, Sr) (Co, Fe)O₃–(Ce, Gd)O₃ composite cathodes. *Solid State Ion* 148:27–34. [https://doi.org/10.1016/S0167-2738\(02\)00102-9](https://doi.org/10.1016/S0167-2738(02)00102-9)
78. Zhou Y, Zhou Z, Song Y, Zhang X, Guan F, Lv H, Liu Q, Miao S, Wang G, Bao X (2018) Enhancing CO₂ electrolysis performance with vanadium-doped perovskite cathode in solid oxide electrolysis cell. *Nano Energy* 50:43–51. <https://doi.org/10.1016/j.nanoen.2018.04.054>
79. Sumi H, Shimada H, Yamaguchi Y, Yamaguchi T, Fujishiro Y (2020) Degradation evaluation by distribution of relaxation times analysis for microtubular solid oxide fuel cells. *Electrochim Acta* 339:135913. <https://doi.org/10.1016/j.electacta.2020.135913>
80. Suzuki T, Awano M, Jasinski P, Petrovsky V, Anderson H (2006) Composite (La, Sr)MnO₃–YSZ cathode for SOFC. *Solid state ion* 177:2071–2074. <https://doi.org/10.1016/j.ssi.2005.12.016>
81. Leonide A (2010) PhD Thesis: SOFC modelling and parameter identification by means of impedance spectroscopy. Karlsruhe Institute of Technology, Karlsruhe, Germany. <https://doi.org/10.5445/KSP/1000019173>. <https://publikationen.bibliothek.kit.edu/1000019173>
82. Ghamarinia M, Babaei A, Zamani C, Aslannejad H (2023) Application of the distribution of relaxation time method in electrochemical analysis of the air electrodes in the SOFC/SOEC devices: a review. *Chem Eng J Adv* 15

Publisher's Note Springer Nature remains neutral with regard to jurisdictional claims in published maps and institutional affiliations.

Springer Nature or its licensor (e.g. a society or other partner) holds exclusive rights to this article under a publishing agreement with the author(s) or other rightsholder(s); author self-archiving of the accepted manuscript version of this article is solely governed by the terms of such publishing agreement and applicable law.